Methods in Ecology and Evolution

BRITISH ECOLOGICAL SOCIETY

Methods in Ecology and Evolution 2017, **8,** 1626–1638 doi: 10.1111/2041-210X.12778

Imaging biological surface topography *in situ* and *in vivo*

Dylan K. Wainwright*[,1], George V. Lauder[1] and James C. Weaver*[,2]

[1]*Museum of Comparative Zoology, and Department of Organismic and Evolutionary Biology, Harvard University, Cambridge, MA 02138, USA; and* [2]*Wyss Institute for Biologically Inspired Engineering, Harvard University, Cambridge, MA 02138, USA*

Summary

1. The creation of accurate three-dimensional reconstructions of biological surfaces is often challenging due to several inherent limitations of current imaging technologies. These include the inability to image living material, requirements for extensive specimen preparation and/or long image acquisition times, and the inability to image at length scales that are relevant for the study of interfacial phenomena that occur between the organism and its environment.

2. In this paper, we demonstrate the use of a new imaging approach that combines the benefits of optical and contact profilometry to image organismal surfaces quickly and without the need for any kind of specimen preparation, thus permitting three-dimensional visualization *in situ*.

3. As a proof of concept, we demonstrate the utility of this approach by imaging the surfaces of a wide range of live and preserved fish and other species, imaging wet, mucus-covered surfaces, and presenting quantitative metrics of surface roughness in a variety of natural and engineered materials.

4. Given the numerous wet, sticky, and slimy surfaces that abound in nature and the importance of the interface between species and their environments for the study of numerous biophysical phenomena, we believe this approach holds considerable promise for providing new insights into surface structural complexity in biological systems.

Key-words: 3D imaging, biology, mucus, profilometry, skin

Introduction

An organism's skin creates a boundary to the external world, and a detailed analysis of this three-dimensional surface structure is important for understanding numerous biophysical phenomena such as gas or moisture transfer, and the generation of drag forces that result from the movement of air and water across these surfaces (Lauder *et al.* 2016). Imaging and quantifying biological surface structural complexity can be accomplished by various methods, including contact and optical profilometry (Salvi *et al.* 2010), atomic force microscopy (AFM; Giessibl 2003), computed tomography (CT; Ritman 2004), confocal microscopy (Stephens 2003), and scanning electron microscopy (SEM; Kessel & Shih 1976). Despite the utility and prevalence of these methods, we currently lack a technique that is useful for the large area and high-throughput generation of three-dimensional surface datasets and is suitable for use with the wet, sticky, or mucus-covered surfaces of living organisms. To meet these needs, the applied method must be rapid, capable of imaging areas in the square millimetre to square centimetre size range, resolve surfaces with high x, y, and z resolution, not require sample preparation, be insensitive to surface optical properties, and be able to image living material. Although confocal microscopy, CT scanning, and AFM can be performed on living tissue, they either have poor surface resolution (CT scanning), sample only small regions (AFM), or are adversely affected by surface properties such as reflectivity (confocal microscopy). In this paper, we demonstrate the use of a gel-based photometric stereo profilometry technique (GelSight (Johnson & Adelson 2009; Johnson *et al.* 2011; Li & Adelson 2013; Li *et al.* 2014; Vetterli, Schmid & Wegener 2014; Lilien 2015; Yuan *et al.* 2015; Vorburger, Song & Petraco 2016)) that fills the aforementioned gap in surface-imaging technologies, and we apply it to a variety of biological surfaces from both living and preserved material.

Gel-based photometric stereo profilometry works by pressing a deformable clear gel pad with one opaque surface (Fig. 1a) onto an object, acquiring a series of photographs (Fig. 1c) from different illumination angles, and combining these images to create a three-dimensional topographical map (Figs 1b and 2). Acquiring the surface images occurs in less than 30 s, and performing a topographical reconstruction of the surface can be accomplished in c. 60 s offline. Additionally, no sample preparation is required and the approach can be routinely performed on live specimens. Wet, slimy, optically clear, or reflective surfaces can be successfully imaged with this approach because the opaquely-coated surface of the clear gel conforms to the specimen, resulting in a uniformly reflective profile that simplifies surface reconstruction.

Gel-based profilometry has been previously used to image surfaces for a variety of engineering applications, including

*Correspondence authors. E-mail: dylanwainwright@fas.harvard.edu, james.weaver@wyss.harvard.edu

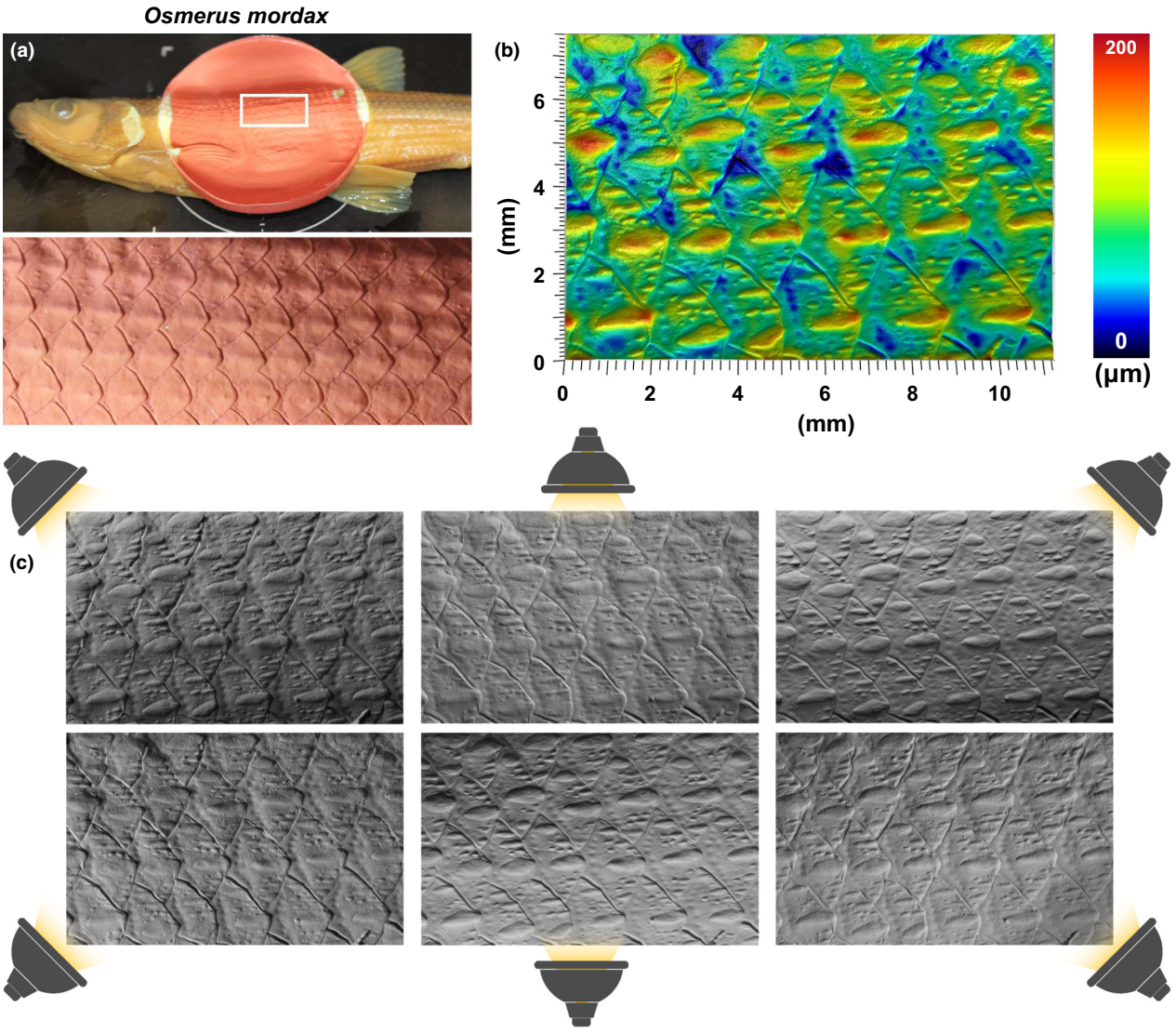

Fig. 1. Gel-based profilometry technique using the GelSight™ method. (a) A smelt (*Osmerus mordax*) is imaged by pressing a clear gel sensor with one coated opaque surface onto an area of interest and then illuminating the impression from six directions. (b) The surface is captured and reconstructed as a height map with known dimensions. Note the bumps which are keratinous breeding tubercles. (c) Each reconstructed surface is generated from six separate images taken with different illumination angles.

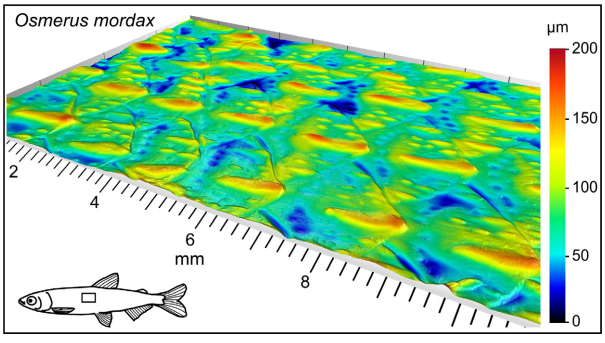

Fig. 2. Oblique view of rainbow smelt (*Osmerus mordax*) surface to highlight the 3D topography of the captured surface data. Scale bar indicates height above the lowest point on this surface.

surface characterization, firearm identification from bullet casings, and robotic sensing of surface texture (Johnson & Adelson 2009; Johnson *et al.* 2011; Li & Adelson 2013; Li *et al.* 2014; Vetterli, Schmid & Wegener 2014; Lilien 2015; Yuan *et al.* 2015), allowing researchers to quantify surface metrology metrics such as roughness, skew, and kurtosis in a high-throughput and noninvasive manner. For biological applications, this method is ideal for answering functional questions regarding surface-environment interactions in aquatic, aerial and arboreal species. Examples include the attachment organs of crustaceans and annelids; aerodynamic and hydrodynamic drag reduction in birds, insects, and fish; and how the scales of agamid lizards and arboreal snakes facilitate climbing. Applying this approach in a biological context, we present 3D surface reconstructions (Fig. 3) with quantitative metrology data (Table 1) from multiple organisms, and demonstrate how this technique can be used on mucus-covered surfaces (Fig. 4). Finally, using fish as a representative sample group, we showcase this technique's ability to capture the *in situ* topography of structurally complex biological surfaces (Figs 1, 2, 4, 5–9).

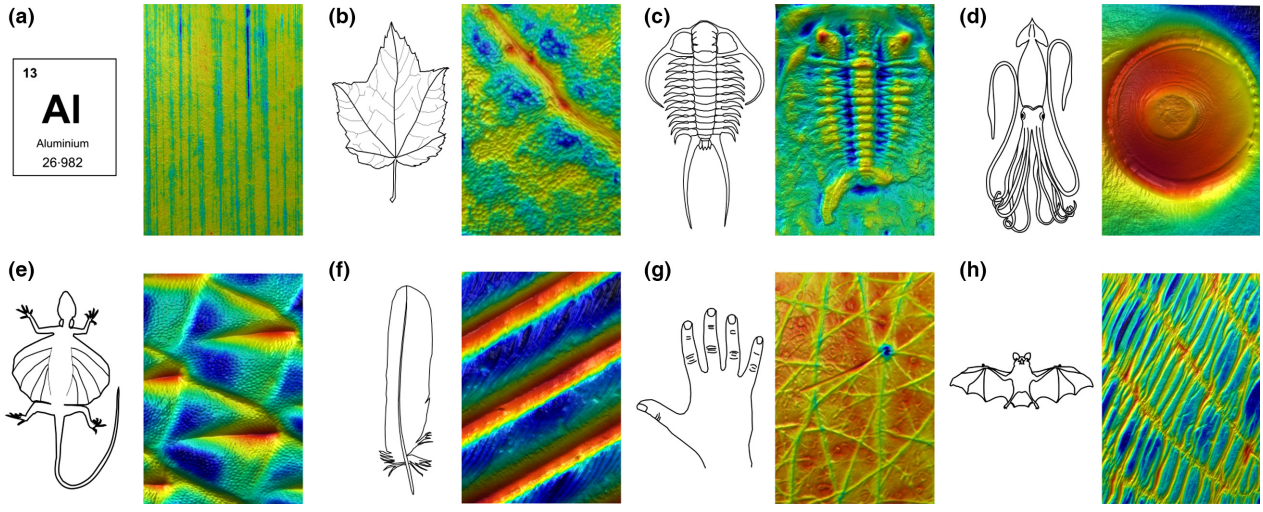

Fig. 3. 3D surface reconstructions using gel-based profilometry. Dimensions given below are image length and width, followed by the distance covered in the *z*-dimension (the elevation of the highest point on the surface). Warm colours correspond to higher, while cool colours correspond to lower elevations (highest: red, lowest: dark blue). (a) extruded aluminum sheet: 1·55 mm × 2·32 mm, *z*: 5 μm. (b) Red maple (*Acer rubrum*) leaf showing vein and cells: 0·73 mm × 1·1 mm, *z*: 31 μm. (c) Trilobite fossil: 14·8 mm × 22·2 mm, *z*: 915 μm. (d) Sucker with enclosed sucker ring from a giant squid (*Architeuthis dux*): 14·8 mm × 22·2 mm, *z*: 3·03 mm. (e) Flying lizard (*Draco timorensis*) belly scales: 0·90 mm × 1·31 mm, *z*: 117 μm. (f) Red-tailed hawk (*Buteo jamaicensis*) feather showing barbs and barbules: 0·75 mm × 1·09 mm, *z*: 152 μm. (g) Back of human hand showing a single hair and pore: 2·89 mm × 4·34 mm, *z*: 86·4 μm. (h) Greater mouse-eared bat (*Myotis myotis*) wing: 6·61 mm × 9·92 mm, *z*: 205 μm.

Table 1. Table of surface metrology parameters for different animals and materials. The table is organized in order of increasing roughness

Surface	Roughness Sq (μm)	Skew Ssk	Kurtosis Sku	Max height Sz (μm)
Aluminium	0·06	−0·20	3·5	6·7
Trout with mucus (*Salmo trutta*)	2·6	0·15	3·3	24·9
Trout preserved (*S. trutta*)	4·4	0·37	2·7	39·1
Hammerhead shark (*Sphyrna zygaena*)	5·2	−0·14	3·1	47·1
1000 grit sandpaper	6·3	0·22	3·1	66·3
Longnose butterflyfish (*Forcipiger flavissimus*)	7·6	0·11	4·1	74·3
Red maple leaf (*Acer rubrum*)	9·1	0·42	4·3	82·1
Back of hand (*Homo sapiens*)	14·3	−0·19	3·5	160·1
500 grit sandpaper	16·2	−0·33	4·5	215·8
Bonefish (*Albula vulpes*)	17·9	0·14	2·9	150·1
Bluegill preserved (*Lepomis macrochirus*)	19·9	−0·50	2·8	137·2
Bluegill with mucus (*L. macrochirus*)	21·7	0·20	2·8	138·7
Flying lizard (*Draco timorensis*)	24·7	0·56	3·2	173·1
Squirrelfish (*Sargocentron spiniferum*)	30·1	−0·11	3·0	235·1
150 grit sandpaper	36·0	0·10	2·8	280·8
80 grit sandpaper	53·6	0·14	2·9	389·7
Bichir (*Polypterus delhezi*)	55·8	−0·04	2·4	349·3
Triggerfish (*Xanthichthys ringens*)	59·8	0·42	3·5	449·2
Trunkfish (*Lactophrys triqueter*)	80·6	0·84	4·1	639·0
Armored catfish (*Hemiancistrus* sp.)	179·3	0·13	2·8	1125·2

Note the synthetic surfaces– aluminium and four grits of sandpaper– interspersed throughout the table as familiar standards.

Materials and methods

GEL-BASED PHOTOMETRIC STEREO PROFILOMETRY TECHNIQUE

Gel-based photometric stereo profilometry works by pressing a deformable clear gel elastomer pad (with one opaque, coated, surface) onto an object, acquiring a series of plan view photographs from different illumination angles, and combining these images to create a topographical map of the surface. For the examples described in this study, we used a system manufactured by GelSight Inc. (Waltham, MA, USA).

Using this approach, it is possible to create 3D reconstructions of a variety of topographically variable surfaces, from extruded aluminium with surface features of less than 5 μm in elevation, to a squid sucker disc with an elevation of 3 mm (Fig. 3a,d). This versatility is due to, but also limited by, the flexibility of the gel sensor that conforms to the surface and the ability of the camera and lens used to image it optically.

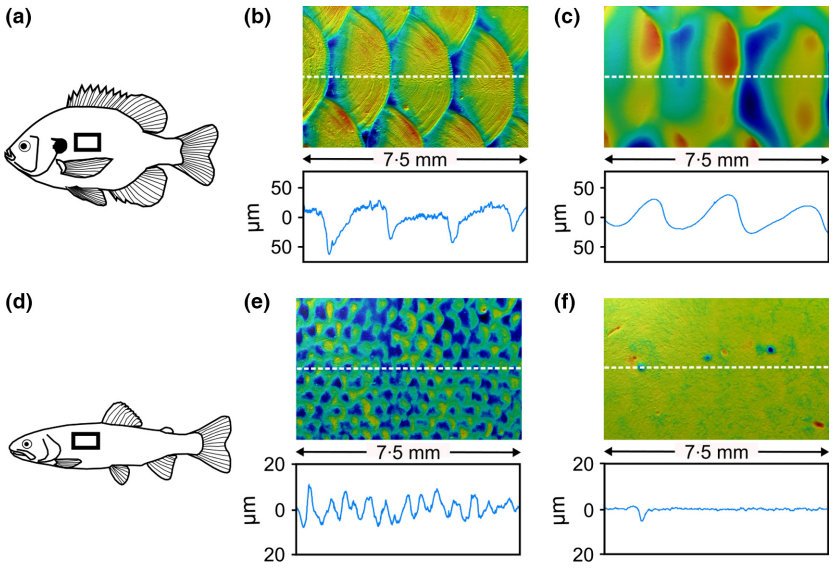

Fig. 4. 3D reconstructions of fish surfaces, with and without mucus. Images in b, c, e, and f are all 7·5 mm × 5 mm. Given below is the distance covered in the *z*-dimension (the elevation of the highest point on the surface). (a) The boxed region illustrates the location that was sampled on a bluegill sunfish (*Lepomis macrochirus*). (b) Image and elevation profile from the surface of a preserved (mucus-free) bluegill, *z*: 137 µm. (c) Image and elevation line-scan profile of an anesthetized (live) bluegill. The presence of mucus covers the microstructural features on the bluegill scales, but does not obscure the overall scale shape, *z*: 89 µm. (d) The boxed region illustrates the location that was sampled on a brown trout, (*Salmo trutta*). (e) Image and elevation line-scan profile from the surface of a preserved (mucus-free) trout, showing small scales, *z*: 39 µm. (f) Image and elevation line-scan profile of an anesthetized (live) trout. The mucus completely obscures the scales and only the lateral line pores are visible, *z*: 11·4 µm.

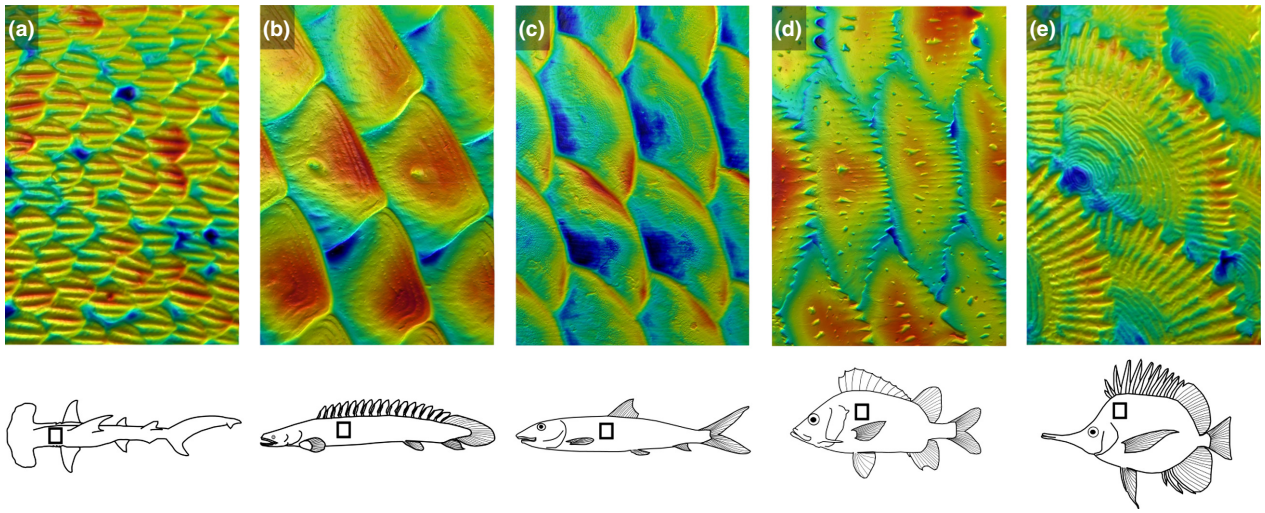

Fig. 5. Common fish scale types. Dimensions given below are image length and width, followed by the distance covered in the *z*-dimension (the elevation of the highest point on the surface). Warm colours correspond to higher, while cool colours correspond to lower elevations. (a) Placoid scales of a smooth hammerhead (*Sphyrna zygaena*): 0·749 mm × 1·09 mm, *z*: 24·5 µm. (b) Ganoid scales of a barred bichir (*Polypterus delhezi*): 7·47 mm × 10·9 mm, *z*: 331 µm. (c) Cycloid scales of a bonefish (*Albula vulpes*): 7·4 mm × 11·1 mm, *z*: 108 µm. (d) Spinoid scales of the sabre squirrelfish (*Sargocentron spiniferum*): 8·2 mm × 11·9 mm, *z*: 181 µm. (e) Ctenoid scales of the yellow longnose butterflyfish (*Forcipiger flavissimus*): 1·26 mm × 1·84 mm, *z*: 36·1 µm.

The standard GelSight system permits the successful imaging of surfaces ranging in dimensions from c. 15 mm × 22 mm to 3 mm × 4·2 mm using different optical zoom settings of the camera lens. Because an 18 megapixel camera is used, each surface is reconstructed with a point density of 18 million 3D (*x*,*y*,*z*) points, permitting the straightforward reconstruction of features down to 5 µm in size.

Gel sensors with different stiffness can be used depending on the specific application. For all of the surfaces imaged here, we used 'soft gels' (R40-XP565:30 SENSOR, Shore 00 30) with a thin opaque layer on one side. While 'soft gel' sensors are good at conforming to both complex and soft surfaces because they deform more easily, these properties also make them more prone to damage, which includes puncturing of the gel's opaque coating. Once a gel sensor becomes damaged, it creates small errors in the scan reconstruction. Although such errors can be corrected through post-processing, for the results reported here, a new gel

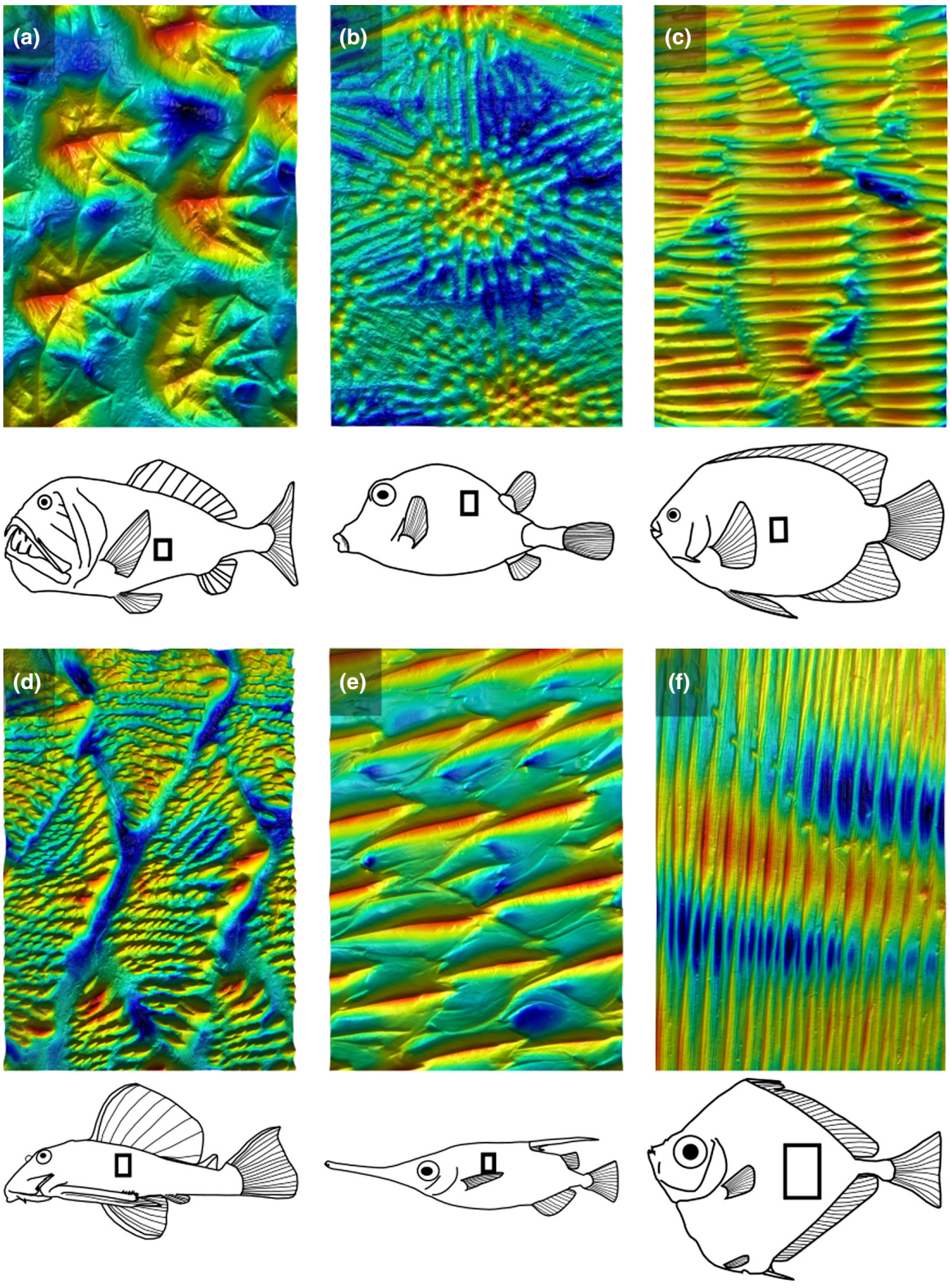

Fig. 6. Fish scale structural diversity. Dimensions given below are image length and width, followed by the distance covered in the *z*-dimension (the elevation of the highest point on the surface). Warm colours correspond to higher, while cool colours correspond to lower elevations. (a) Fangtooth (*Anoplogaster cornuta*): 1·89 mm × 2·83 mm, *z*: 392 μm. (b) Smooth trunkfish (*Lactophrys triqueter*): 14·8 mm × 22·2 mm, *z*: 337 μm. (c) King angelfish (*Holacanthus passer*): 3·72 mm × 5·43 mm, *z*: 184 μm. (d) Suckermouth armored catfish (*Hemiancistrus* sp.): 6·81 mm × 10 mm, *z*: 1·13 mm. (e) Longspine snipefish (*Macroramphosus scolopax*): 1·9 mm × 2·77 mm, *z*: 142 μm. (f) Spotted tinselfish (*Xenolepidichthys dalgleishi*): 9·22 mm × 13·6 mm, *z*: 388 μm.

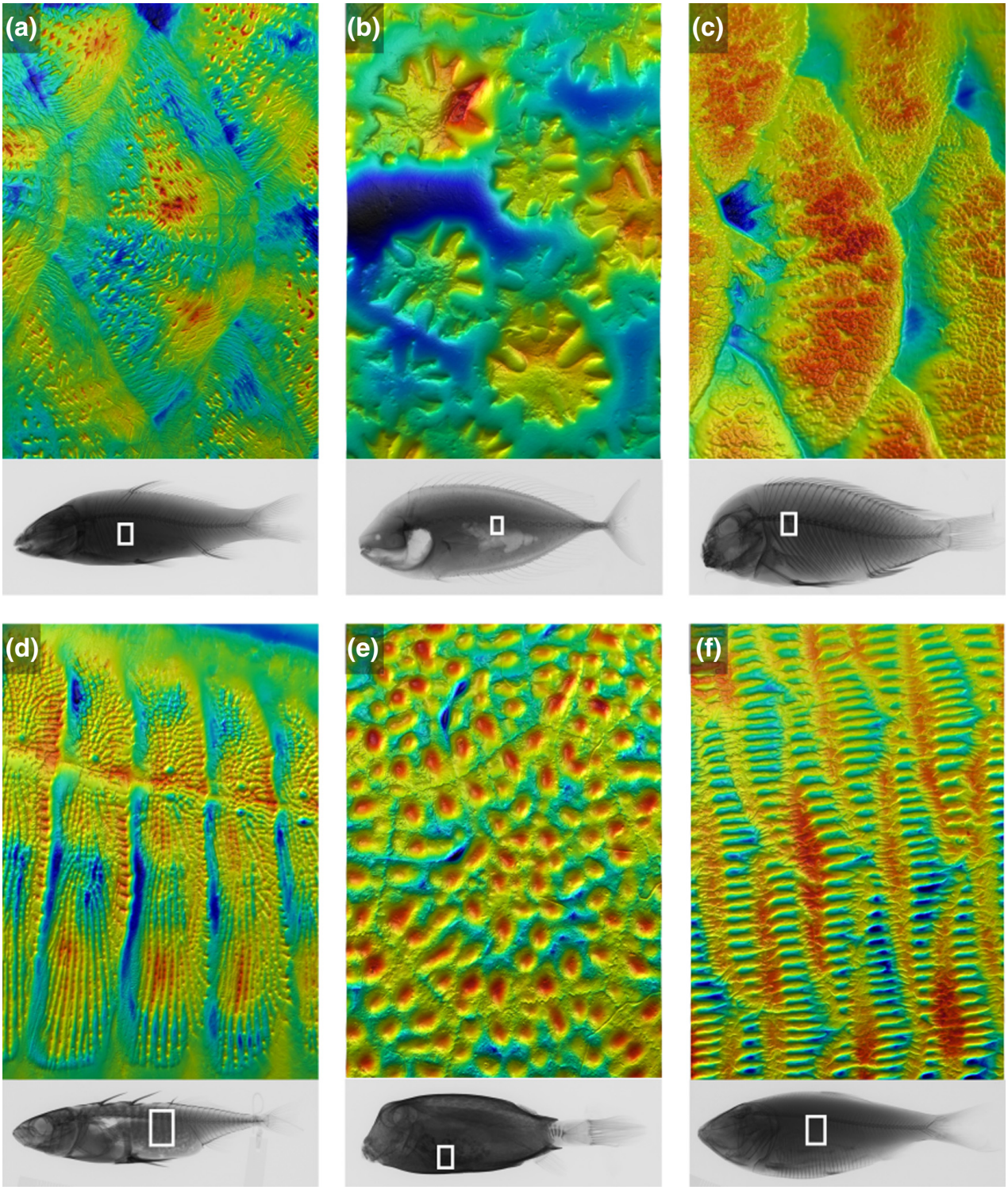

Fig. 7. Surface diversity of fish scales and scale-like tissues accompanied by whole specimen x-ray images with boxed regions of interest. Dimensions given below are image length and width, followed by the distance covered in the *z*-dimension (the elevation of the highest point on the surface). Warm colours correspond to higher, while cool colours correspond to lower elevations. (a) Carp (*Cyprinus carpio*): 8·96 mm × 11·5 mm, *z*: 121 μm. (b) Louvar (*Luvaris imperialis*): 1·9 mm × 2·77 mm, *z*: 130 μm. (**c**) *Tropheus moorei*: 4·94 mm × 7·2 mm, *z*: 258 μm. (d) Stickleback (*Gasterosteus aculeatus*): 8·94 mm × 11·5 mm, *z*: 180 μm. (e) Boxfish (*Ostracion meleagris*): 5·14 mm × 7·49 mm, *z*: 191 μm. (f) Menhaden (*Brevoortia patronus*): 7·4 mm × 10·8 mm, *z*: 133 μm.

was used after the first detected sign of surface damage. As a result, the number of uses per gel sensor is dependent on the surfaces being imaged as well as the gel type being used. For example, imaging flat surfaces with gentle curves can be performed hundreds of times without the need for gel sensor replacement.

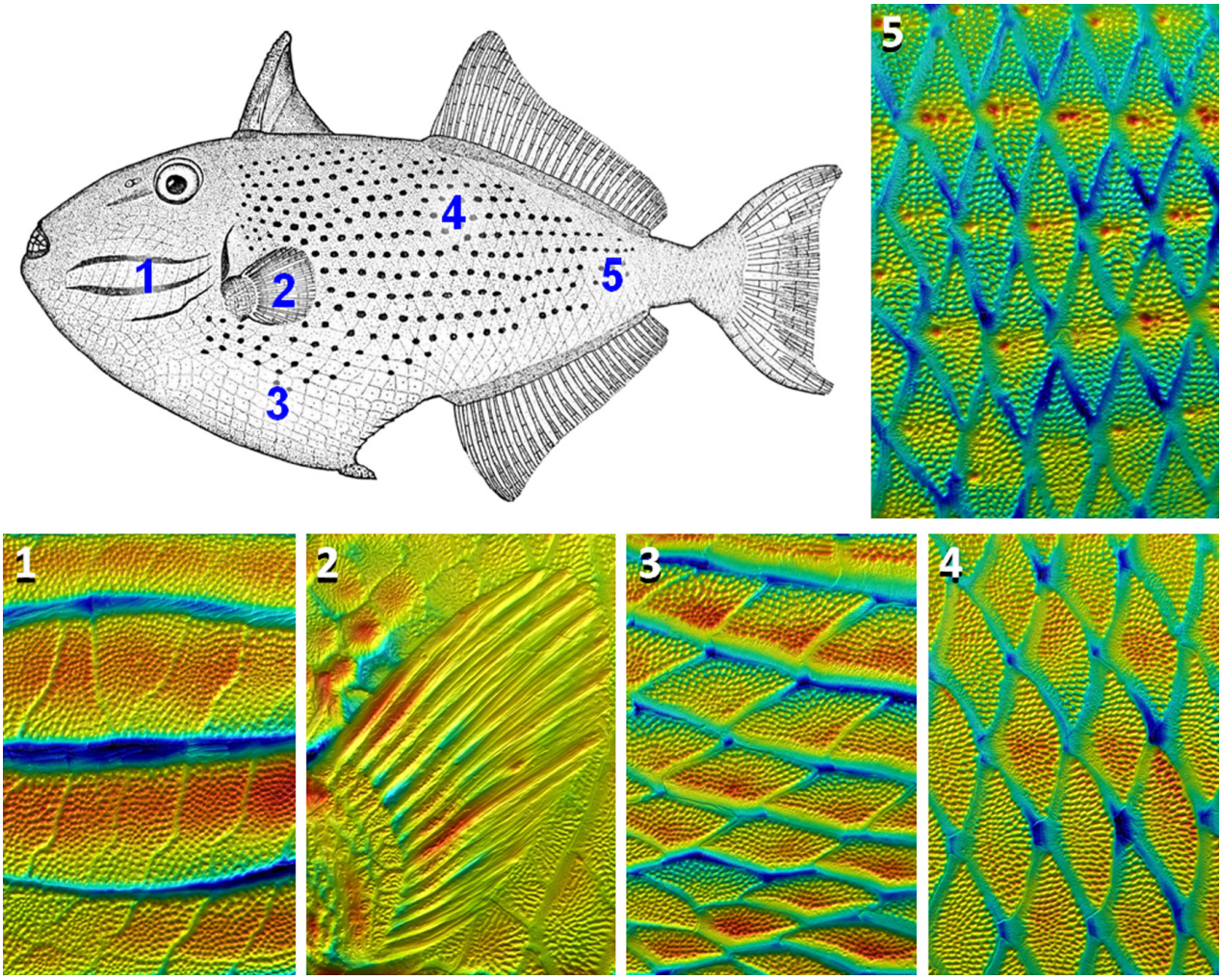

Fig. 8. Surface and scale diversity across the body of the sargassum triggerfish (*Xanthichthys ringens*). All images measure 14·8 mm × 22·2 mm and have the same orientation relative to the body. Warm colours correspond to higher, while cool colours correspond to lower elevations. Below we also give the distance covered in the *z*-dimension (the elevation of the highest point on the surface). 1: Ventral to the eye; *z*: 775 μm, 2: Pectoral fin, *z*: 925 μm, 3: Ventral to the pectoral fin, note the apparent 90° rotation of scales, *z*: 440 μm, 4: Ventral to the start of the second dorsal fin, *z*: 375 μm, 5: Between the end of the second dorsal and anal fin, *z*: 449 μm. Triggerfish image adapted from (Randall, Matsuura & Zama 1978).

A standard DSLR camera was used to acquire the source images from the different illumination angles, and for each combination of gel sensor type and camera setting, a unique calibration file is generated and used for surface reconstruction. For the samples described here, we used one gel type ('soft gel' R40-XP565:30 SENSOR, Shore 00 30) and standardized camera settings for each lens zoom level. The major trade-off we encountered was between the depth of field and shutter speed. Ideally, the depth of field should be as large as possible to image surfaces with large elevation changes, but this leads to longer exposure times, especially at higher zooms. To minimize movement of both the camera and the specimen during long image acquisitions, we used a shutter delay on the camera and limited foot traffic and other disturbances near our imaging system. After image acquisition, the 3D surface reconstructions were generated using the Gelsight Software (GSCapture Version 0.7).

IMAGING MUCUS

One unique application of gel-based profilometry is in the imaging of surfaces covered with viscous liquids such as mucus. Figure 4 shows examples of mucus imaging in two species of fish, the bluegill (*Lepomis macrochirus*) and the brown trout (*Salmo trutta*). These images were taken by anesthetizing an individual of each species using tricaine methanesulfonate (MS-222) under Harvard IACUC protocol 20-03 to GVL, and then immediately imaging the skin surface. For mucus imaging, we used 'soft gel' (R40-XP565:30 SENSOR, Shore 00 30) sensors and gently moved the gel into contact with the anesthetized fish. We found that even with moderate pressure between the gel sensor and the anesthetized fish, the integrity of the mucus layer was largely unaffected.

SPECIMENS IMAGED

Most of the preserved specimens imaged in this paper were selected from the Museum of Comparative Zoology (MCZ), Department of Ichthyology biodiversity collection. Each specimen was used with permission from the museum and their MCZ specimen numbers are given in Table S1, Supporting Information. No damage was done to the specimens imaged, as gel-based profilometry is a non-destructive technique for most applications. Because this technique applies light pressure to the surface of interest, we have found that wet specimens, such as fish preserved in ethanol, are often easier to image than dry animal

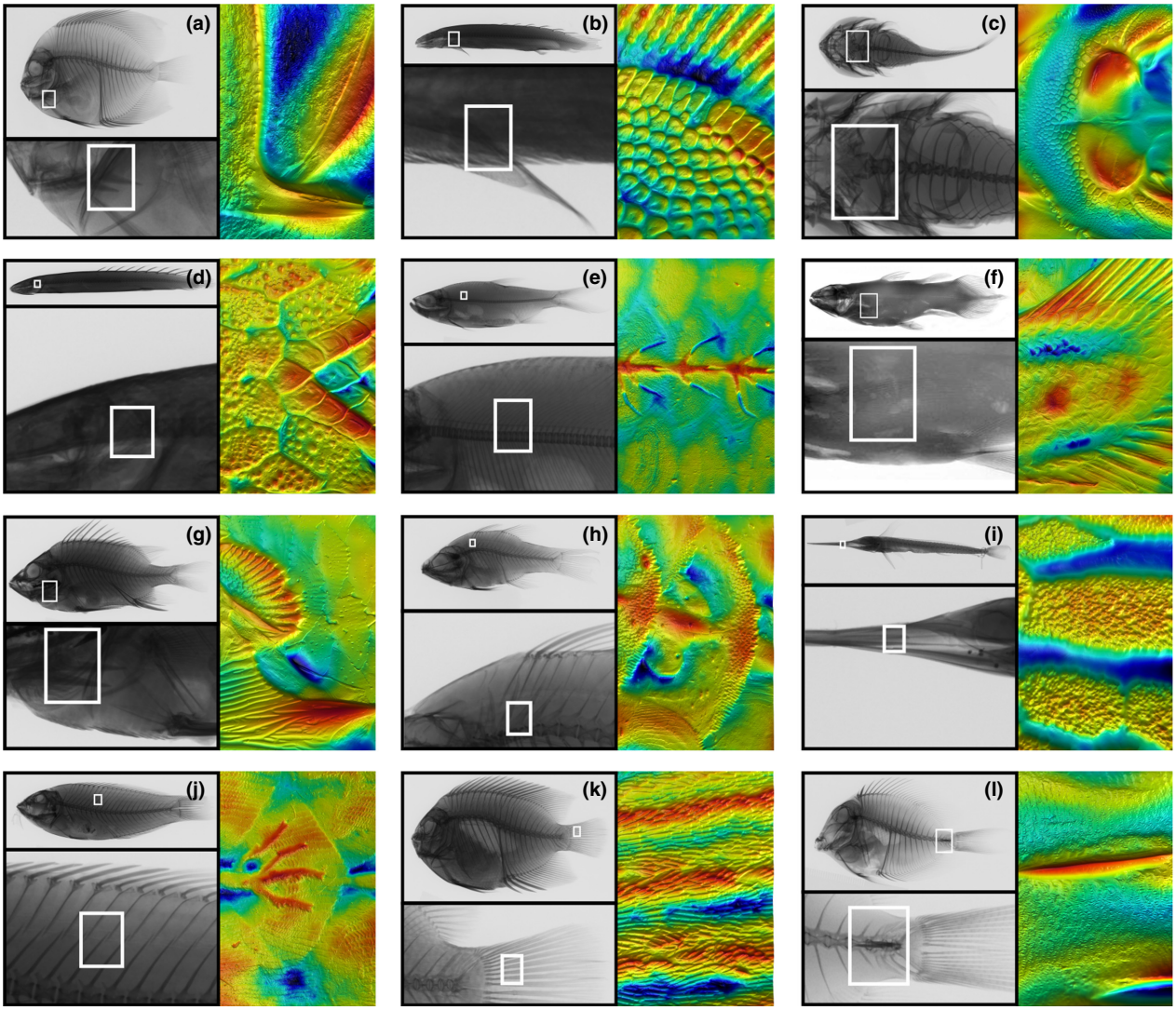

Fig. 9. Surface structural diversity in fishes accompanied by whole specimen x-ray images with boxed regions of interest. Dimensions given below are image length and width, followed by the distance covered in the *z*-dimension (the elevation of the highest point on the surface). Warm colours correspond to higher, while cool colours correspond to lower elevations (a) Gray angelfish (*Pomacanthus arcuatus*) preopercular spine: 7·45 mm × 10·9 mm, *z*: 1240 μm. (b) Barred bichir (*Polypterus delhezi*) pectoral fin: 5·14 mm × 7·12 mm, *z*: 285 μm. (c) Clingfish (*Gobiesox maeandricus*) adhesive disc derived from fused pelvic fins: 13 mm × 21·1 mm, *z*: 1340 μm. (d) Saddled bichir (*Polypterus endlicheri*) dorsal view of head: 14·8 mm × 22·2 mm, *z*: 976 μm. (e) Tarpon lateral line scales (*Megalops cyprinoides*): 7·5 mm × 9·96 mm, *z*: 152 μm. (f) Coelacanth (*Latimeria chalumnae*) pectoral fin: 13·8 mm × 20·4 mm, *z*: 496 μm. X-ray from Smithsonian National Museum of Natural History X-ray vision: Fish inside out series. (g) Sabre squirrelfish (*Sargocentron spiniferum*) preopercular spines: 13·7 mm × 18·2 mm, *z*: 1004 μm. (h) Cardinalfish lateral line (*Apogon imberbis*): 2·88 × 4·46 mm, *z*: 184 μm. (i) Striped marlin (*Kajikia audax*) teeth on the dentary: 5 mm × 7·5 mm, *z*: 532 μm. (j) Christmas wrasse (*Thalassoma trilobatum*) lateral line scales: 7·8 mm × 6 mm, *z*: 212 μm. (k) King angelfish (*Holacanthus passer*) tail scales: 3·72 mm × 5·4 mm, *z*: 214 μm. (l) Striated surgeonfish (*Ctenochaetus striatus*) scalpel on caudal peduncle: 5·6 mm × 7·8 mm, *z*: 931 μm.

material, which tends to be more brittle and less flexible, making it difficult to position specimens for imaging.

SURFACE ANALYSIS

Fish and other organisms often have curved surfaces, and when comparing surface textures among different regions or in species with different degrees of overall body curvature, it is necessary to remove this global curvature to reveal and compare local topographic features. We performed this background subtraction step in the Mountains Map software (Mountains Map 7.2.7344, Digital Surf, Besançon, France) using the 'remove form' function with varying polynomial complexities. Mountains Map software was also used to calculate the reported surface metrology parameters (Table 1), perform linear measurements in *x*, *y*, and *z* dimensions, and produce images of the surfaces.

Results

IMAGING SURFACE TOPOGRAPHY

Using gel-based profilometry, we have successfully imaged a diversity of surfaces, ranging from sandpaper and aluminium, to fossils, human skin, feathers, bat wings, and the mucus

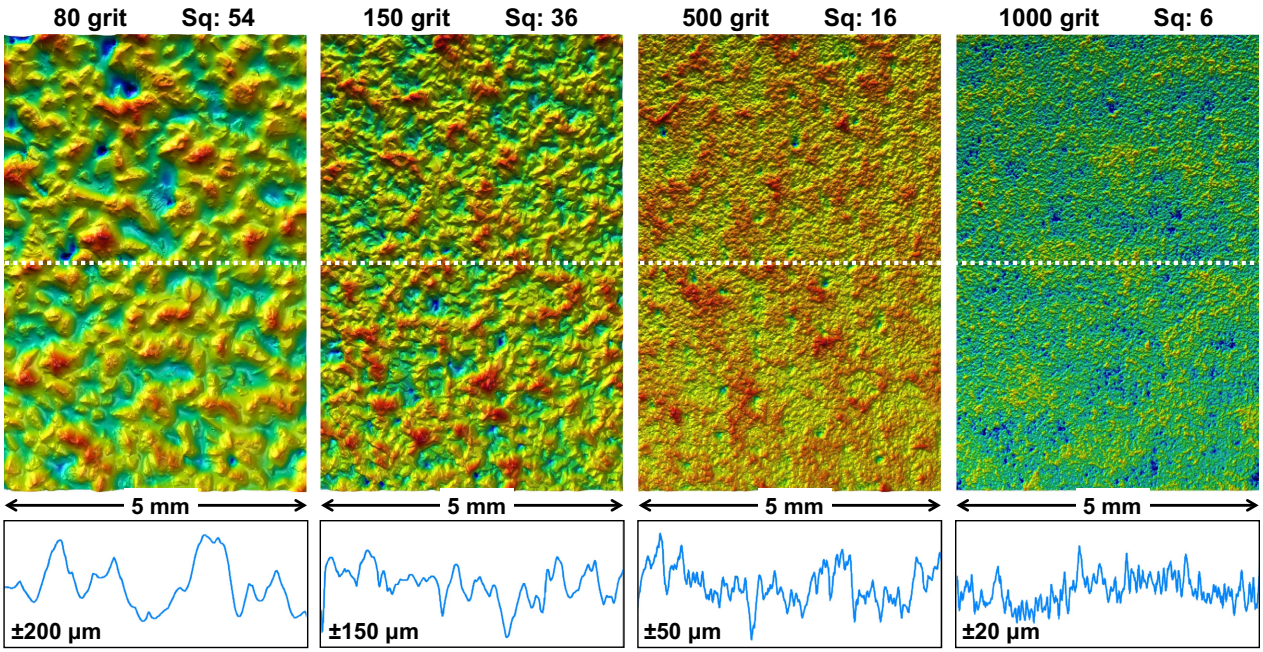

Fig. 10. Surface reconstructions of commercially available sandpapers (ranging from 80 grit to 1000 grit) to illustrate gel-based topographic imaging of known materials. All images are 5 mm × 7·5 mm with a corresponding elevation profile. Below we also give the distance covered in the *z*-dimension (the elevation of the highest point on the surface). Sq indicates root mean square surface roughness. (a) 80 grit sandpaper, *z*: 390 µm. (b) 150 grit sandpaper, *z*: 281 µm. (c) 500 grit sandpaper, *z*: 216 µm. (d) 1000 grit sandpaper, *z*: 66 µm.

coatings of living fish (Figs 3 and 4). All figures presented here illustrate elevation reconstructions performed using GelSight and MountainsMap software, where warmer colours correspond to higher elevations. Due to the wide range of surface roughness exhibited by the specimens used in this study, each image has a different elevation scale and the maximum elevation for each image is indicated in the figure captions.

Figure 3 illustrates a diversity of surfaces imaged with gel-based profilometry and demonstrates the versatility of this approach. While the aluminum sample is smooth to the touch, surface profilometry clearly reveals small (5 µm in elevation) parallel surface ridges resulting from extrusion manufacturing (Fig. 3a). Surface images of a red maple leaf show distinct individual cell boundaries, and leaf veins with elongated cells (Fig. 3b). An image of a hawk feather (Fig. 3f) reveals its characteristic barbs and barbules, with hooks (or hamuli) on the individual barbules. Figure 3g features human skin from one of the coauthors, clearly showing the voronoi-like organization of dead epidermal cells. For all of these examples, not only can small structural features be distinguished, but relative elevations can also be measured to address functional hypotheses (Table 1).

Panels c, d, e, and h in Fig. 3 illustrate applications of gel-based photometry for larger scan areas. The trilobite fossil (Fig. 3c) demonstrates non-destructive imaging of fossilized material. The giant squid sucker ring (Fig. 3d) clearly shows both the outer (infundibulum) and inner (acetabulum) (Kier & Smith 1990) sucker zones and the relatively low profile sucker ring teeth, and the flying lizard skin in Fig. 3e shows large keels present on each scale. Flying lizards are notoriously good climbers and these keels are directed posteriorly, perhaps serving as hooks or friction-increasing elements to reduce slipping. It is also possible that the keels and general scale morphology serve a complementary aerodynamic function during aerial gliding. Finally, the bat wing membrane (Fig. 3h) shows the structure of muscles and the associated connective tissue. The muscles are the smoother fibres oriented from the lower left to the upper right of the image and the connective tissue are the more kinked lines running in the opposite orientation (Skulborstad, Swartz & Goulbourne 2015). This organization of muscles and elastic fibres allows the bat wing to be both flexible and controllable (Skulborstad, Swartz & Goulbourne 2015).

IMAGING MUCUS-COVERED SURFACES

To demonstrate the advantages of this approach for investigating biologically relevant surface topography in living systems, we compared the 3D surface profiles from both fresh and preserved specimens of bluegill (*L. macrochirus*) and brown trout (*S. trutta*). The mucus-free specimens were formalin-fixed and preserved in ethanol at the Museum of Comparative Zoology (Harvard University) (Fig. 4b,e) and were compared to live, anesthetized individuals maintained in our laboratory (Fig. 4c,f).

Initial observations from the studies on preserved specimens reveal the dramatic size difference in scales between the two species, with the visible length of the bluegill scales being c. 3·5× those of the brown trout. The size difference in scales between the two species likely has a profound effect on how the scales interact with the surrounding water in the living fish. As predicted from the small size of trout scales (measuring

c. 15 μm in elevation), 3D reconstructions of the mucus-covered anesthetized fish revealed that the scales are completely obscured by the mucus layer, with the lateral line pores being the only surface features still visible (Fig. 4d–f) in the living specimens.

In contrast, bluegill have much larger scales that protrude c. 50 μm above the skin surface, and even in mucus-covered fish, the individual scales can still be distinguished. While the gross morphological features of the bluegill scales (size, shape and relative elevation) are clearly visible and similar in both live and preserved specimens (as revealed in corresponding line profiles), the structural details of the scales are completely obscured by the surface mucus in the living fish, raising intriguing questions as to functional significance of the scales' spines, ridges, and striations.

QUANTIFYING BIOLOGICAL SURFACES

Using 3D reconstructions obtained from both biological and engineered materials, we compared their surface roughness metrics in Table 1, organized by increasing roughness. Roughness (root-mean-square roughness, Sq), is given by the square-root of the sum across the surface of the squared distance of each point from the mean height. Skew (Ssk) and kurtosis (Sku) are parameters concerning the shape of the distribution of heights across a surface. A normal distribution of heights results in a skew of zero and a kurtosis of three. High positive skew corresponds to surfaces with many tall peaks, while low, negative skew describes surfaces with many deep valleys. A kurtosis above three indicates extremely high peaks or valleys, while a kurtosis below three indicates relatively gradual (and non-extreme) surface curvatures.

For this metrology parameter comparative study, we also included a wide range of commercially available sandpapers (ranging from 80 grit to 1000 grit) as familiar internal standards (see Fig. 10 for sandpaper surface images). From these measurements, the dramatic difference in fish surface roughness among the various taxa examined is readily apparent, which spans nearly two orders of magnitude.

The brown trout (Fig. 4b) was the smoothest fish measured, and unsurprisingly, the live specimen (with mucus) exhibited only half the roughness of its preserved counterpart (without mucus). The lone elasmobranch, the hammerhead shark (Fig. 5a), exhibited a similarly low surface roughness due to its very small placoid scales (compared to those found in most other ray-finned fish species). Both the trout and the hammerhead shark surfaces were both close in roughness to 1000 grit sandpaper, along with the scales of the longnose butterflyfish (Fig. 5e) and the surface of the red maple leaf (Fig. 3b). The next grouping of surface measurements, which were close to that of 500 grit sandpaper, included skin on the back of a human hand (Fig. 3g), bonefish scales (Fig. 5c), and the bluegill, both with and without mucus (Fig. 4a). While, for the different specimens examined, bluegill sunfish with mucus exhibited a higher roughness value than the bluegill without mucus, the difference was small (<2 μm, or about 10% of the roughness values), and could likely be due to the slight size differences between the two imaged specimens. The scales of the flying lizard (Fig. 3e) exhibited the next highest roughness values, followed by squirrelfish scales (Fig. 5d) and 150 grit sandpaper, 80 grit sandpaper, the ganoid scales of the bichir fish (Fig. 5b), and those of the sargassum triggerfish (Fig. 8). Trunkfish scales exhibited c. 20 μm greater roughness than the triggerfish, while the protective plates of armored catfish were over twice as rough as the trunkfish. Many of the fish with the roughest scales are traditionally categorized of as heavily armored fishes, with scales likely performing more of a protective rather than a hydrodynamic function.

None of the mapped surfaces exhibited particularly extreme values for skew, with most of these surfaces having an approximately normal distribution of heights. There were two surfaces with somewhat negative (about −0·5) skew values, the bluegill scales without mucus and the 500 grit sandpaper, due to the repeated occurrence of valley features on these surfaces. The red maple, and the scales of the flying lizard, triggerfish, and trunkfish, all had somewhat positive skew values (c. 0·5), indicating the presence of pronounced protruding features such as peaks, keeled scales, and leaf veins. Most surfaces also exhibited kurtosis values close to three, indicating a lack of extreme peaks or valleys. The few surfaces with high kurtosis values were the longnose butterflyfish scales, the red maple leaf, 500 grit sandpaper, and the trunkfish scales (kurtosis >4). These higher kurtosis values indicate more extreme surface features, such as the elevated leaf vein on an otherwise smooth leaf surface. In the results table, we also included values for the highest relative elevation (maximum height, Sz) on each surface, which largely followed the trends in measured roughness.

FISH SURFACE DIVERSITY: A CASE STUDY

As an example of a class of biological surfaces that illustrate the utility of *in situ* and *in vivo* gel-based surface profilometry measurements, we present data on a diverse assemblage of fish surfaces, which reveal remarkable variation both between species and on the body of single individuals. Quantifying the interface between fish and their fluid environment is critical for specific analyses of boundary layer structure (Anderson, McGillis & Grosenbaugh 2001; Dean & Bhushan 2010), and the general hydrodynamics of locomotion (Lauder & Tytell 2005). In order to obtain useful information regarding the structural complexity of fish scales, the surfaces must be imaged in a manner which allows analysis of areas on the order of 1 cm^2, because individual scales overlap and form complex patterns that generate intricate topography (Lauder *et al.* 2016; Wainwright & Lauder 2016). Smaller analysis regions miss the larger topographic arrangements that result from among-scale patterning.

Figures 4, and 5–9 illustrate the remarkable diversity of fish scale morphologies. Fish scales have been studied for more than a century and have been categorized and used for species identification and to inform the evolutionary relationships among different species (Agassiz 1833; Roberts 1993). Fish scales are also useful for aging purposes (Beardsley 1967; Park

& Lee 1988), for distinguishing different populations (Margraf & Riley 1993; Ibañez, Cowx & O'Higgins 2007), and for the identification of species from gut contents, middens, or the fossil record (Shackleton 1987; Daniels 1996). Historically, fish scales have been grouped into separate categories based on their external and internal morphological features (Agassiz 1833) and here, we present images of the five most common scale types among extant cartilaginous and ray-finned fishes (Fig. 5) using gel-based profilometry.

The placoid scales of sharks and rays are illustrated in Fig. 5a. These scales are typically very small (c. 100–200 μm long) and sit atop pedestals that grow from anchors in the skin (Motta *et al*. 2012). In many sharks, placoid scales form densely overlapping patterns (Fig. 5a), which have been shown to reduce drag and increase thrust under turbulent boundary layer conditions (Dean & Bhushan 2010; Oeffner & Lauder 2012). From our measurements, individual placoid scales are clearly visible, as well as the individual raised riblets on each scale, which have been hypothesized to play an important role in drag reduction.

While elasmobranch scales are all categorized as placoid, the scales of bony fishes have been further categorized, and here we provide examples of ganoid, cycloid, spinoid, and ctenoid scales (Fig. 5). Figure 5b shows the ganoid scales of a bichir, which are rhomboidal in shape and are characterized by a layer of hard ganoine covering their outer surface (Sire & Huysseune 2003). These scales interlock with pegs and sockets on each scale to create a flexible, but tough tile-like coating that has recently provided inspiration for the development of biomimetic armor (Duro-Royo *et al*. 2015). The two central scales in Fig. 5b are lateral line scales, with small pores that open to the lateral line canal where sensory hair cells measure water flow. Lateral line scales of different morphologies are also clearly visible in other imaged species (Fig. 9e,h,j).

Most bony fish have elasmoid scales, which have lost the hard ganoine layer and are instead composed of only two layers – an outer bony layer and an inner layer of connective tissue (Sire & Akimenko 2004). Elasmoid scales have been further categorized into cycloid, crenate, ctenoid, and spinoid forms based on the morphology of their posterior margins (Roberts 1993). Cycloid scales have smooth edges, and we show scales of a bonefish as an example (Fig. 5c). Figure 5d shows spinoid scales from a squirrelfish, with spines that are continuous with the body of each scale (and not separate ossifications). Finally, Fig. 5e shows the ctenoid scales of a butterflyfish, defined by the interlocking spines at the posterior margin, which are independent ossifications from the main body of each scale.

Figure 6 illustrates some extreme scale types ranging from the enlarged hexagonal plate-like scales of a boxfish, to the small, almost placoid-like scales of the fangtooth and snipefish, and the dorsoventrally elongated scales of the deepwater tinselfish. Figure 7 shows even more diversity of scale types in fishes, including cycloid and spinoid scales, as well as some highly modified morphologies that defy classification (Fig. 7b). In addition to scales, we also present surfaces of other interesting fish features, such as modified fins for surface attachment, protective head armour, lateral line pores, and spines (Fig. 9).

SCALE DIVERSITY WITHIN AN INDIVIDUAL

To investigate the diversity of scale surface topography across a single individual, we imaged the surface of the sargassum triggerfish, *Xanthichthys ringens* (Fig. 8), a planktivorous species from the tropical and sub-tropical Western Atlantic. Examining five different areas of the body: the cheek, belly, pectoral fin, and the regions below the dorsal fin and near the caudal peduncle, our results demonstrate dramatic region-specific variability in scale size, morphology, orientation, spacing, surface roughness, and aspect ratio across a single specimen.

Discussion

The ability to rapidly image the surface topography of biological specimens, both living and preserved, illustrates the unique capabilities of gel-based profilometry to generate data relevant to key questions regarding the surface roughness of biological tissues. Although other techniques exist for investigating biological surfaces (SEM, CT, AFM, etc.), gel-based profilometry has unique benefits which include the lack of specimen preparation, fast image acquisition time, and the ability to capture 3D surface details in the mm^2 to cm^2 size range of wet, reflective, or transparent materials.

Measuring the topography of mucus-covered surfaces (Fig. 4) is a unique and valuable capability of this imaging approach. Mucus has been proposed to perform an important immune function in fish (Shephard 1994; Roberts & Powell 2005; Subramanian, Ross & MacKinnon 2008), and some evidence suggests that fish mucus may also serve to reduce drag in some species (Bernadsky, Sar & Rosenberg 1993; Shephard 1994). As such, the ability to successfully image mucus coatings in living fish is important for assessing both health and swimming performance. In our live fish imaging studies (Fig. 4), we show that there appear to be complex interactions between scale size and associated mucus coats that creates a spectrum of different surfaces among species. As demonstrated, trout have small scales (10–15 μm elevation) that become undetectable when imaged *in vivo* with their mucus coating intact (Fig. 4d–f). In contrast, bluegill have much larger scales (30–60 μm elevation) that are still evident through the mucus coat, although lower amplitude surface elements become obscured (Fig. 4a–c).

Gel-based profilometry also permits the quantification of biological 3D surface metrics (Table 1). The ability to accurately measure surfaces in a size range relevant to many interfacial interactions allows for statistical analysis and comparative studies to be performed in a relevant way. By utilizing traditional metrology metrics such as roughness, skew, and kurtosis, we can compare biological surfaces to each other and to engineered surfaces (Table 1).

While the examples provided here represent applications for which this imaging approach is ideally suited, this

technique does have its limitations. In particular, gel-based profilometry is not well suited for generating realistic 3D reconstructions of protruding filamentous or large spiny structures, small diameter holes, or overhangs. It flattens filaments, cannot focus on the entire depth of long spines or conform to narrow holes, and cannot reconstruct undercuts or overhangs. Despite these limitations, as shown from the examples provided here, gel-based profilometry can be applied to address many research questions in the biological and physical sciences. For example, a long-standing hypothesis about the functional significance of different scale types seen across fish species surmises that spiny scales profoundly alter the boundary layer around fish to decrease drag (Bone 1972; Aleyev 1977; Burdak 1986; Helfman *et al*. 2009; Wainwright & Lauder 2016). Although it has been shown that the placoid scales of some sharks (Fig. 5a) can reduce drag and increase thrust under certain conditions (Oeffner & Lauder 2012), the same has not been shown for the scales of bony fish. As demonstrated here, fish scales show a tremendous amount of diversity both between taxa (Figs 5–7, 9) and on an individual (Fig. 8), yet no study has shown a connection between this structural diversity and hydrodynamic effects. Gel-based profilometry can supply us with accurate reconstructions of fish and other biological surfaces, which in turn, can be used in computational fluid dynamic models or as the basis for creating physical models via 3D printing for direct experimental studies. Indeed, any biological surfaces that come into contact with a substrate or a surrounding fluid can profoundly affect swimming, flying, running, jumping, or climbing, and understanding the three-dimensional topography of these surfaces is a critical step in assessing interfacial phenomena in biomechanics.

Authors' contributions

D.K.W., G.V.L., and J.C.W. conceived the ideas; D.K.W. collected and analysed the data and led the writing of the manuscript. All authors contributed critically to the drafts, and gave final approval for publication.

Acknowledgements

The authors are grateful to Kimo Johnson (GelSight, Inc.) for his imaging advice. This research on fishes was approved under Harvard IACUC 20-03. Our work was supported by ONR MURI Grant No. N000141410533 monitored by Bob Brizzolara to G.V.L., NSF GRF DGE-1144152 to D.K.W., and an HFSP Young Investigators Grant (RGY0067-2013) to J.C.W.

Data accessibility

All data used in this paper is included in the manuscript itself. Each image includes a height scale that is listed in the caption and the quantitative data we discuss is present in Table 1.

References

Agassiz, L. (1833) *Recherches sur les poissons fossiles: Tome 2*. Petitpierre, Neuchatel, Switzerland.

Aleyev, Y.G. (1977) *Nekton*. Dr. W. Junk b.v. Publishers, The Hague, the Netherlands.

Anderson, E.J., McGillis, W.R. & Grosenbaugh, M.A. (2001) The boundary layer of swimming fish. *The Journal of Experimental Biology*, **204**, 81–102.

Beardsley, G.L. (1967) Age, growth, and reproduction of the Dolphin, *Coryphaena hippurus*, in the Straits of Florida. *Copeia*, **1967**, 441.

Bernadsky, G., Sar, N. & Rosenberg, E. (1993) Drag reduction of fish skin mucus: relationship to mode of swimming and size. *Journal of Fish Biology*, **42**, 797–800.

Bone, Q. (1972) Buoyancy and hydrodynamic functions of integument in the Castor Oil Fish, *Ruvettus pretiosus* (Pisces: Gempylidae). *Copeia*, **1972**, 78–87.

Burdak, V.D. (1986) Morphologie fonctionnelle du tegument ecailleux des poissons. *Cybium*, **10**, 1–128.

Daniels, R.A. (1996) Guide to the identification of scales of inland fishes of northeastern North America. *New York State Museum Bulletin*, **488**, 1–93.

Dean, B. & Bhushan, B. (2010) Shark-skin surfaces for fluid-drag reduction in turbulent flow: a review. *Philosophical Transactions. Series A, Mathematical, Physical, and Engineering Sciences*, **368**, 4775–4806.

Duro-Royo, J., Zolotovsky, K., Mogas-Soldevila, L., Varshney, S., Oxman, N., Boyce, M.C. & Ortiz, C. (2015) MetaMesh: a hierarchical computational model for design and fabrication of biomimetic armored surfaces. *CAD Computer Aided Design*, **60**, 14–27.

Giessibl, F.J. (2003) Advances in atomic force microscopy. *Reviews of Modern Physics*, **75**, 949–983.

Helfman, G.S., Collette, B.B., Facey, D.E. & Bowen, B.W. (2009) *The Diversity of Fishes*, 2nd edn. John Wiley and Sons Inc., Hoboken, NJ, USA.

Ibañez, A.L., Cowx, I.G. & O'Higgins, P. (2007) Geometric morphometric analysis of fish scales for identifying genera, species, and local populations within the Mugilidae. *Canadian Journal of Fisheries and Aquatic Sciences*, **64**, 1091–1100.

Johnson, M.K. & Adelson, E.H. (2009) Retrographic sensing for the measurement of surface texture and shape. *IEEE Conference on Computer Vision and Pattern Recognition*, **2009**, 1070–1077.

Johnson, M.K., Cole, F., Raj, A. & Adelson, E.H. (2011). Microgeometry capture using an elastomeric sensor. *ACM SIGGRAPH 2011 Papers on – SIGGRAPH '11*, 1–8.

Kessel, R.G. & Shih, C.Y. (1976) *Scanning Electron Microscopy in Biology: A Students' Atlas on Biological Organization*, 1st edn. Springer-Verlag, Berlin, Heidelberg, Germany; New York, NY, USA.

Kier, W.M. & Smith, A.M. (1990) The morphology and mechanics of octopus suckers. *Biological Bulletin*, **178**, 126–136.

Lauder, G.V. & Tytell, E.D. (2005) Hydrodynamics of undulatory propulsion. *Fish Physiology*, **23**, 425–468.

Lauder, G.V., Wainwright, D.K., Domel, A.G., Weaver, J., Wen, L. & Bertoldi, K. (2016) Structure, biomimetics, and fluid dynamics of fish skin surfaces. *Physical Review Fluids*, **1**, 060502-1–060502-18.

Li, R. & Adelson, E.H. (2013) Sensing and recognizing surface textures using a GelSight sensor. *IEEE Conference on Computer Vision and Pattern Recognition*, **2013**, 1241–1247.

Li, R., Platt, R.J., Wenzhen, Y., Pas, A., Roscup, N., Srinivasan, M.A. & Adelson, E. (2014) Localization and manipulation of small parts using GelSight tactile sensing. *International Conference on Intelligent Robots and Systems*, **2014**, 3988–3993.

Lilien, R. (2015) *Applied Research and Development of a Three-Dimensional Topography System for Firearm Identification Using GelSight*. Acton, MA, USA.

Margraf, F.J. & Riley, L.M. (1993) Evaluation of scale shape for identifying spawning stocks of coastal Atlantic striped bass (*Morone saxatilis*). *Fisheries Research*, **18**, 163–172.

Motta, P., Habegger, M.L., Lang, A., Hueter, R. & Davis, J. (2012) Scale morphology and flexibility in the shortfin mako *Isurus oxyrinchus* and the blacktip shark *Carcharhinus limbatus*. *Journal of Morphology*, **273**, 1096–1110.

Oeffner, J. & Lauder, G.V. (2012) The hydrodynamic function of shark skin and two biomimetic applications. *The Journal of Experimental Biology*, **215**, 785–795.

Park, E.-H. & Lee, S.-H. (1988) Scale growth and squamation chronology for the laboratory-reared hermaphroditic fish *Rivulus marmoratus* (Cyprinodontidae). *Japanese Journal of Ichthyology*, **34**, 476–482.

Randall, J.E., Matsuura, K. & Zama, a. (1978) A revision of the triggerfish genus Xanthichthys, with description of a new species. *Bulletin of Marine Science*, **28**, 688–706.

Ritman, E.L. (2004) Micro-computed tomography – current status and developments. *Annual Review of Biomedical Engineering*, **6**, 185–208.

Roberts, C.D. (1993) Comparative morphology of spined scales and their phylogenetic significance in the Teleostei. *Bulletin of Marine Science*, **52**, 60–113.

Roberts, S.D. & Powell, M.D. (2005) The viscosity and glycoprotein biochemistry of salmonid mucus varies with species, salinity and the presence of amoebic gill

disease. *Journal of Comparative Physiology B: Biochemical, Systemic, and Environmental Physiology*, **175**, 1–11.
Salvi, J., Fernandez, S., Pribanic, T. & Llado, X. (2010) A state of the art in structured light patterns for surface profilometry. *Pattern Recognition*, **43**, 2666–2680.
Shackleton, L.Y. (1987) A comparative study of fossil fish scales from three upwelling regions. *South African Journal of Marine Science*, **5**, 79–84.
Shephard, K.L. (1994) Functions for fish mucus. *Reviews in Fish Biology and Fisheries*, **4**, 401–429.
Sire, J.-Y. & Akimenko, M.-A. (2004) Scale development in fish: a review, with description of sonic hedgehog (shh) expression in the zebrafish (*Danio rerio*). *The International Journal of Developmental Biology*, **48**, 233–247.
Sire, J.-Y. & Huysseune, A. (2003) Formation of dermal skeletal and dental tissues in fish: a comparative and evolutionary approach. *Biological Reviews of the Cambridge Philosophical Society*, **78**, 219–249.
Skulborstad, A.J., Swartz, S.M. & Goulbourne, N.C. (2015) Biaxial mechanical characterization of bat wing skin. *Bioinspiration & Biomimetics*, **10**, 36004.
Stephens, D.J. (2003) Light microscopy techniques for live cell imaging. *Science (New York, NY)*, **300**, 82–86.
Subramanian, S., Ross, N.W. & MacKinnon, S.L. (2008) Comparison of antimicrobial activity in the epidermal mucus extracts of fish. *Comparative Biochemistry and Physiology – B Biochemistry and Molecular Biology*, **150**, 85–92.
Vetterli, M., Schmid, M. & Wegener, K. (2014) Comprehensive investigation of surface characterization methods for laser sintered parts. *Proceedings of the Fraunhofer Direct Digital Manufacturing Conference*, **2014**, 1–6.
Vorburger, T.V., Song, J. & Petraco, N. (2016) Topography measurements and applications in ballistics and tool mark. *Surface Topography: Metrology and Properties*, **4**, 1–52.
Wainwright, D.K. & Lauder, G.V. (2016) Three-dimensional analysis of scale morphology in bluegill sunfish, *Lepomis macrochirus*. *Zoology*, **119**, 182–195.
Yuan, W., Li, R., Srinivasan, M.A. & Adelson, E.H. (2015). Measurement of shear and slip with a GelSight tactile sensor. *2015 IEEE International Conference on Robotics and Automation (ICRA)*, **2015**, pp. 304–311.

Received 11 November 2016; accepted 22 March 2017
Handling Editor: Erica Leder

Supporting Information

Details of electronic Supporting Information are provided below.

Table S1. Museum specimen identification numbers.